Experimental investigation of state-selective single and double electron capture in slow C^{5+}-He collisions

Hualin Zhang, X. Fléchard, A. Cassimi, L. Adoui, F. Frémont, D. Lecler, G. Cremer, L. Guillaume, D. Lelievre, A. Lepoutre, and D. Hennecart

Centre Interdisciplinaire de Recherche Ions-Lasers, CEA/CNRS/ISMRA/Université de Caen Basse Normandie, Rue Claude Bloch, Boîte Postale 5133, F-14070 Caen Cedex 5, France

(Received 5 March 1999)

Single and double electron capture in $C^{5+}+He$ collisions at energies ranging from 9 to 90 keV have been investigated using recoil ion momentum spectroscopy. Doubly differential cross-section measurements allow the identification of the processes involved in the electron transfer. For single capture, *n*-state relative populations and projectile scattering angle distributions are given and compared to previous calculations. A satisfying simple model calculation is proposed. The cross sections for the transfer excitation process are found to be smaller than the calculated cross sections. In the case of double capture, the autoionizing double capture dominates and populates the symmetric state $C^{3+}(2l2l')$, while the true double capture mainly gives rise to $C^{3+}(2lnl')$ $(n>2)$ configurations. In addition to experimental relative populations and stabilization ratios, the *Q*-value resolution enables us to show the processes involved in the population of the different $(2l2l')$ terms. These processes, which are correlated double capture and correlated transfer excitation, are found to depend strongly on the collision energy. [S1050-2947(99)00911-7]

PACS number(s): 34.70.+e, 34.50.Fa

I. INTRODUCTION

Single and double electron capture have been heavily studied in recent decades. Recoil ion momentum spectroscopy (RIMS) has been proven to be a relevant technique to study the electron capture process with refined details on an unprecedentedly achieved energy range [1,2]. One of its prominent merits is that it can identify the final states in spite of whether the projectile is charged or neutral after the collision [3]. This technique has renewed the interest for such studies and should lead to a better understanding of the different interactions participating in the electron transfer [4]. The electron-electron interaction, which is difficult to take into account in the calculation, has recently been the subject of three theoretical studies concerning C^{5+} on He collisions [5–7]. Single and double capture cross sections have been calculated either in the framework of a semiclassical close-coupling description [6] or a simple coupled-channel model with correlated double capture states [7]. Discrepancies between these two calculations arise due to an improved representation of the 1*s* core, according to [6]. The authors [6] were also able to derive transfer-excitation (TE) cross sections, which is a two-electron process.

Experimental data are too scarce to allow much comparison with these theoretical predictions. Up to now, only partial results have been given [8–15]. The single capture (SC) is thus known to populate mainly $n=3$ state from translational energy gain experiments [10] and photon spectroscopy [11]. Concerning double electron capture, only the autoionizing double capture (ADC) has been studied by electron spectroscopy and the populated configurations identified [12–15]. However, no complete set of data concerning SC, ADC, and true double capture (TDC) relative cross sections for populating the different configurations and projectile scattering angle exists. The aim of this work is thus to provide a further discussion of SC, ADC, and TDC in light of experimental doubly differential cross sections obtained by RIMS in the energy range 9–90 keV. After a description of the experimental setup, we will discuss our results concerning the following processes:

$$\begin{aligned} C^{5+}+He &\rightarrow C^{4+*}+He^{+}, \quad \text{SC}, \\ &\rightarrow C^{4+*}+He^{+*}, \quad \text{TE}, \end{aligned} \tag{1}$$

$$\begin{aligned} C^{5+}+He &\rightarrow C^{3+*}+He^{2+} \rightarrow C^{4+}+He^{2+}+e, \quad \text{ADC}, \\ &\rightarrow C^{3+*}+He^{2+} \rightarrow C^{3+}+He^{2+}+h\nu, \quad \text{TDC}. \end{aligned} \tag{2}$$

We compare our data to our calculation, to calculations of Fritsch and Lin [6] and Hansen and Taulbjerg [7], and also to the measurement of Khemliche *et al.* [15].

II. EXPERIMENTAL SETUP

The C^{5+} projectile is provided by a 14 GHz electron cyclotron resonance (ECR) ion source of the Grand Accélérateur National D'Ions Lourds (GANIL, Caen, France) [16]. The beam is collimated by a 600 μm aperture located at the entrance of the spectrometer and two pairs of slits 3 m upstream. The ion beam crosses the target supersonic jet at the center of the spectrometer. In the first generation of RIMS, uniform electric fields were used and the resolution was limited by the geometrical dimensions of the collision region (overlap between the ion beam and the supersonic gas jet) [1]. The momentum resolution has been improved by using a nonuniform electric field to extract the recoil ions and focuses ions with the same velocity on the position sensitive detector, whatever the starting point [17]. The extraction region is followed by a field-free region in order to ensure the time focusing condition [1]. Finally, the recoil ions are post-

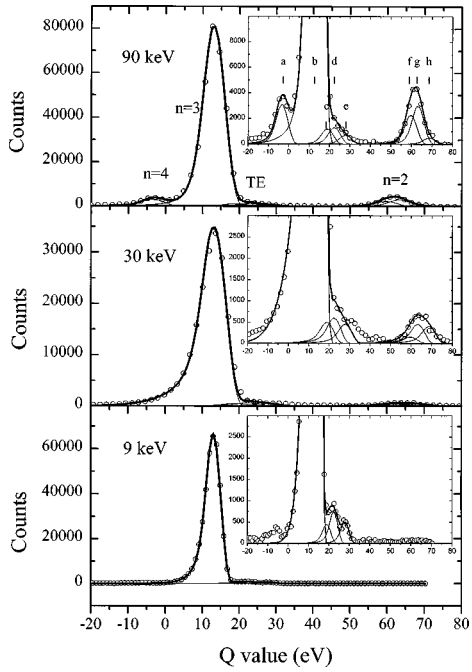

FIG. 1. Experimental single capture Q-value spectra for the C^{5+}-He system. The different configurations $(a,b,c,\ldots)$ and corresponding Q values are given in Table I.

accelerated toward the detector, so that the detection efficiency is independent of the charge state of the ion. After the collision, the projectile ions are charge-analyzed using an electrostatic deflector associated with a second position sensitive detector. For each capture event, the time of flight and the impact position of the recoil ion together with the projectile position are recorded by a list mode data acquisition. The two first quantities give access directly to the recoil ion longitudinal $P_{R\parallel}$ and transverse $P_{R\perp}$ momentum components.

The principle of RIMS relies on the relationship between the recoil ion momentum and two important quantities: the Q value of the reaction and the projectile scattering angle θ.

Kinetically, the capture process may be viewed as an inelastic two-body collision. It is thus straightforward to show that, for small scattering angles,

$$Q=-P_{R\parallel}V_p-\frac{n_cV_p^2}{2}, \tag{3}$$

TABLE I. Different configurations and Q values involved in single electron capture and transfer excitation for the C^{5+}-He system.

Peak	Configuration	Q value (eV)	Process
a	$C^{4+}1s4l$	-3.4	SC
b	$C^{4+}1s3p(^1P^0)$,$C^{4+}1s3d(^3D)$, $C^{4+}1s3s(^3S)$	13.02	SC
c	$C^{4+}1s2p(^1P)+He^{1+}2l$	18.89	TE
d	$C^{4+}1s2p(^3P)+He^{1+}2l$	22.38	TE
e	$C^{4+}1s2s(^3S)+He^{1+}2l$	27.82	TE
f	$C^{4+}1s2p(^1P^0)$	59.68	SC
g	$C^{4+}1s2p(^3P^0)$	63.2	SC
h	$C^{4+}1s2s(^3S)$	68.6	SC

TABLE II. Experimental SC relative cross sections for the C^{5+}-He collision (%).

Peak	State	90 keV	30 keV	9 keV
f,g,h	$n=2$	6.2 ± 0.5	2.7 ± 0.7	0 ± 0.4
b	$n=3$	87.1 ± 3.7	93.2 ± 4.1	97.5 ± 3.1
a	$n=4$	3.3 ± 1.3	0.0 ± 0.5	0.0 ± 0.4
c,d,e	TE	3.4 ± 2.4	4.1 ± 1.9	2.5 ± 1.8

$$\theta=\frac{P_{R\perp}}{P_0}. \tag{4}$$

$P_{R\parallel}(P_{R\perp})$ is the recoil ion longitudinal (transverse) momentum. P_0 is the projectile longitudinal momentum, V_p is the velocity of the projectile, and n_c is the number of captured electrons. The Q value corresponds to the potential energy released as the kinetic energy and thus contains information on the state populated on the projectile by the capture process. In the particular case of C^{5+} on He, the resolution is high enough to separate different configurations. It reached resolutions [full width at half maximum (FWHM)] of 4.5 eV for single capture and 7.4 eV for double capture.

The calibration of the Q-value spectra is deduced first through the geometrical characteristics of the spectrometer. Then, since the Q-value spectra are made of well-separated peaks, the calibration and identification are refined using the state energies calculated, in our case, with the code of Cowan [18].

III. RESULTS AND DISCUSSION

In this section, we present experimental relative differential cross sections and projectile scattering angle distributions for single capture, transfer excitation, and double capture, and a theoretical calculation for single capture. Three sets of data are given corresponding to C^{5+} on He at 9, 30, and 90 keV collision energy. The cross sections are derived from the Q-value spectra after a fitting procedure, in which the line shape corresponds to the spectrometer response (determined from a pure and separated single capture peak) and the line position is imposed to the theoretical expectation. Great care

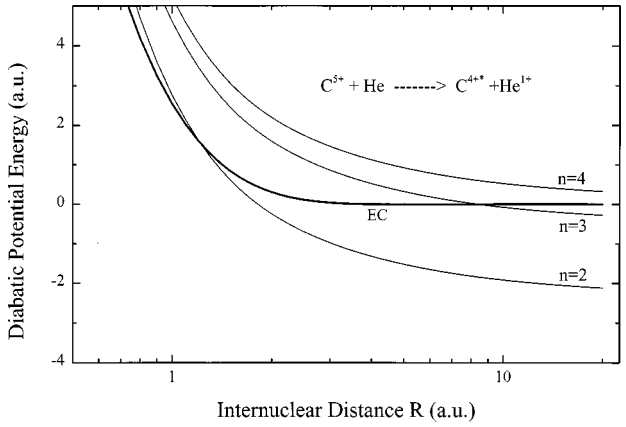

FIG. 2. Diabatic potential curves of SC for the C^{5+}-He system. EC is the entrance channel.

TABLE III. SC theoretical results (relative cross section excluding TE) compared to experimental values for the C^{5+}-He collision (%).

		90 keV		30 keV		9 keV	
Peak	State	Expt.	Theory	Expt.	Theory	Expt.	Theory
f,g,h	$n=2$	6.5 ± 0.5	6.42	2.8 ± 0.7	1.44	0.0 ± 0.4	0.005
b	$n=3$	90.1 ± 3.8	90.91	97.2 ± 4.3	98.07	100 ± 3.2	99.99
a	$n=4$	3.4 ± 1.3	2.67	0.0 ± 0.5	0.49	0.0 ± 0.4	0.008

has been taken in the calculation of errors, the origins of which are the collection efficiency correction, deconvolution, statistics, and background substraction.

A. Single electron capture (SC)

From the *Q*-value spectra (Fig. 1), for the different configurations (listed in Table I), the differential cross sections populated during the collision were extracted (Table II). The spectra show that RIMS is able to give information not only on the configurations but also on the relative intensities of the terms involved in the capture process (Fig. 1).

More than 87% of the single capture takes place in the *M* shell $C^{4+}(3l)$ as predicted by current models (Landau-Zener calculation [19], over the barrier model [20]), and already observed by [10]. Also visible in the spectra (Fig. 1), the reaction window width increases as the collision energy is raised [21]: Capture in the *L* shell $[C^{4+}(2l)]$ and *N* shell $[C^{4+}(4l)]$ gains importance from 9 to 90 keV.

The electron capture on the $C^{4+}(4l)$ state may not be understood in the Landau-Zener image of the collision since no crossing exists between the $n=4$ and the entrance channels (Fig. 2). We developed a simple coupled channel calculation in order to reproduce the population of this state. Comparison of the experimental and calculated scattering angle distributions should shed light on the location of the transition.

In this model, the diabatic potentials taken into account are

$$V_1(R)=-\frac{\alpha q^2}{2R^4}[1-\exp(\beta R)]^4+\frac{Z_{\mathrm{He}}q}{R}\times\exp(-\kappa_1 R),\quad \text{entrance channel (EC)}, \tag{5}$$

$$V_n(R)=\frac{(q-1)}{R}+\frac{Z_{\mathrm{He}}(q-1)}{R}\times\exp(-\kappa_F R)-Q(n),\quad \text{SC into n state}. \tag{6}$$

A Meyer-Born type repulsive potential is used to account for the core-core interaction at short internuclear distance, where $\kappa_1=\sqrt{2U_1^T}$ and $\kappa_F=\sqrt{2U_2^T}$, U_1^T and U_2^T are the ionization potential of He and He^+, $Q(n)$ is the *Q* value for the *n* state, Z_{He} is the nuclear charge of He ($Z_{\mathrm{He}}=2$), and *q* is the charge of the projectile ($q=5$).

Polarization energy is included in the entrance channel (EC), in which $\alpha=1.375a_0^3$ is the polarizability of the helium atom and $\beta=0.28a_0^{-1}$ [22] is a ''cutoff'' parameter introduced to avoid the divergence of the polarization potential at small internuclear distance *R*. These diabatic potential curves are given in Fig. 2. The EC crosses the $n=3$ channel at about 8 a.u. and the $n=2$ channel at about 1.5 a.u., but does not cross the $n=4$ channel except at very small internuclear distance where these diabatic potential curves fail to depict the real situation.

The exchange interactions are taken from Olson and Salop [23]:

$$H_{ij}=\left(\frac{9.13}{\sqrt{q}}\right)\exp\left[-13.324R\left(\frac{2U_1^T}{q}\right)^{1/2}\right]. \tag{7}$$

The formula was derived to estimate the coupling interaction at the crossing R_c of a single electron capture energy curve with the initial-state energy curve. Such a formula is used here for $R\neq R_c$. Provided *R* is not too small, some justification is obtained from the fact that in the asymptotic region H_{ij} behaves as $R^a e^{-bR}$ (*a* and *b* are constants) [24], which is dominated by the exponential term.

The interactions H_{ij} correspond to the following elements of the interaction matrix:

$$\begin{array}{c} \\ \mathrm{EC} \\ n=2 \\ n=3 \\ n=4 \end{array}\begin{array}{c} \begin{array}{cccc} \mathrm{EC} & n=2 & n=3 & n=4 \end{array} \\ \begin{pmatrix} V_1 & H_{12} & H_{13} & H_{14} \\ H_{12} & V_2 & 0 & 0 \\ H_{13} & 0 & V_3 & 0 \\ H_{14} & 0 & 0 & V_4 \end{pmatrix} \end{array}. \tag{8}$$

In order to evaluate each contribution to the SC process, we solved the four coupled-channel equations in the framework of the impact parameter method using the PAMPA code [25]. The radial coupling, the rotational coupling, and the

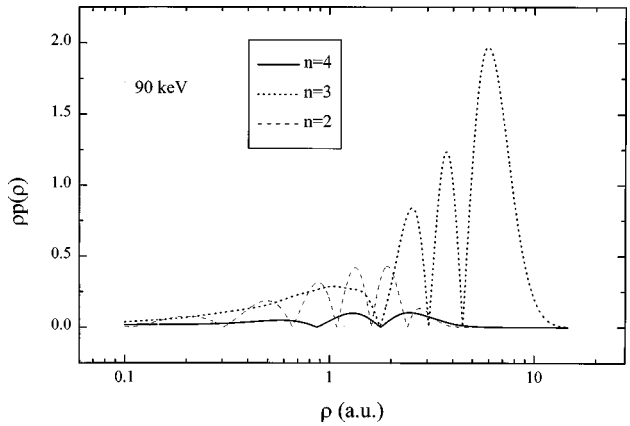

FIG. 3. Impact parameter (ρ) dependent SC transition probabilities $\rho P(\rho)$ calculated within our model for the C^{5+}-He system at 90 keV collision energy.

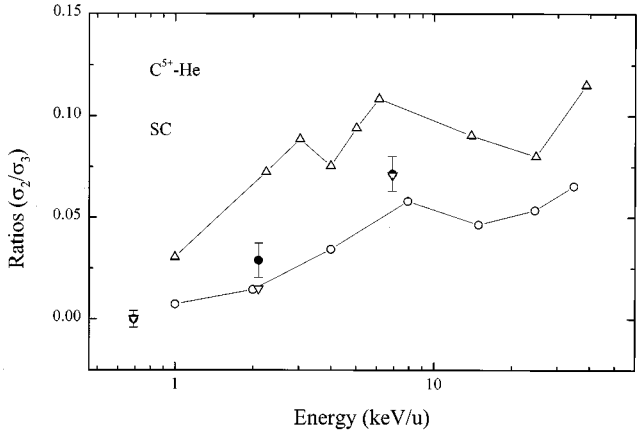

FIG. 4. Cross section ratios between $n=2$ and 3 single capture for the C^{5+}-He system. ●, our experimental data; ∇, calculation by our model; ○, Fritsch and Lin [6]; △, Tauljberg and Hansen [7].

electron translation factor were neglected. The calculation results are compared with our experimental values in Table III. The good agreement for the cross sections allows some confidence for the calculated scattering angle distributions.

The transition probability to the $n=4$ state is predicted to take place at small impact parameters (1–3 a.u.) (Fig. 3). For $n=2$ and 3, the maximum probability agrees with the location of the curve crossings (Fig. 2).

A first test is to compare the experimental ratio of the highest capture cross sections, namely $\sigma(n=2)/\sigma(n=3)$ (without TE, which has not been taken into account by Hansen and Taulbjerg [7]), to the calculations [6,7] and this model. Figure 4 shows that the measurements lie in between the theoretical predictions obtained by Fritsch and Lin [6], Hansen and Taulbjerg [7], and our simple model.

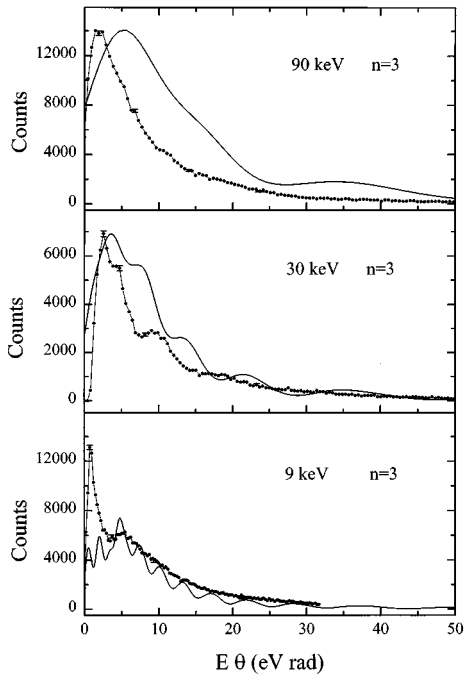

FIG. 5. Projectile scattering angle distribution of the SC $C^{4+}(3l)$ channel. The full lines are the results calculated within our model. **E** is the collision energy; θ is the projectile scattering angle.

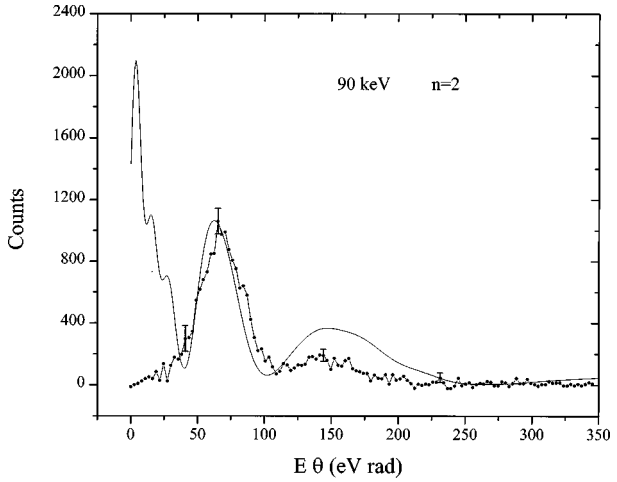

FIG. 6. Same as Fig. 5 for the $C^{4+}(2l)$ channel.

Our model also gives the scattering angle distribution, which may be compared to the experimental measurements. For the main channel, capture in $C^{4+}(3l)$, a good agreement is shown in Fig. 5. An oscillatory behavior is evidenced by the distribution at 30 keV, which is also reproduced by our simple model. These oscillations correspond to interference between different pathways and are known as Stuckelberg oscillations [26].

Figure 6 shows the same comparison for capture on the $C^{4+}(2l)$ state at 90 keV. Two peaks are observed in agreement with the model prediction. The prediction by our simple model does not work for small $E\theta$ values. This scheme could be due to the competition between the single and double capture channel. The profound mechanism involved in this angular distribution should be explored by a further theoretical calculation, which should simultaneously include single and double electron capture in the model.

Capture in $C^{4+}(4l)$ is observed only at 90 keV. Again our angle distribution calculation is in rather good agreement with the measurement (Fig. 7). The peaks visible in the distribution are much wider than for the $n=3$ channel. This behavior is not surprising since the $n=4$ energy curve does not cross the entrance channel; there is no localized crossing between these two curves. The measured angle (large value) confirms the predicted population of this state at small impact parameters (Fig. 3).

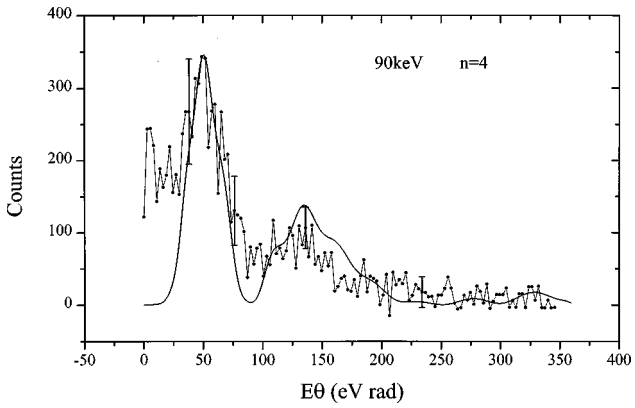

FIG. 7. Same as Fig. 5 for the $C^{4+}(4l)$ channel.

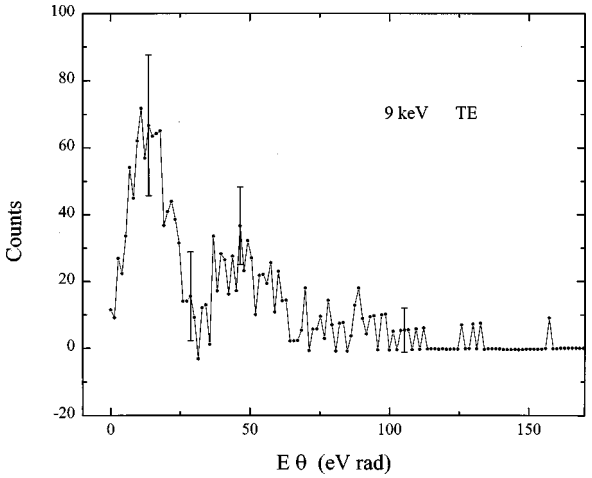

FIG. 8. Projectile scattering angle distribution for the transfer excitation $[C^{4+}(2l)+He^{+}(2l')]$ channel.

B. Transfer excitation (TE)

Another process is evidenced by the experimental spectra. The transfer excitation (TE), a two-electron process, corresponds to the capture of one electron on the projectile $C^{4+}(2l)$ with excitation of the remaining target electron $He^{+}(2l')$ in our case. The associated relative cross section does not change much with the collision energy (2.5% at 9 keV, 4.1% at 30 keV, and 3.4% at 90 keV) (Table II). This process has been estimated theoretically [6], but higher values have been presented (8.7% at 9 keV, 9.7% at 30 keV, and 11.4% at 90 keV). In this calculation, the authors mentioned that TE takes place mainly at a small impact parameter (0.1–1.3 a.u.). In this impact parameter range, the results must be very sensitive to the description of the projectile $1s$ core, which may play an important role at such small internuclear distances. Thus, it seems not to be correct enough to take into account the $1s$ electron only through a model potential.

The TE scattering angle distribution shows large scattering angles associated to small impact parameters (Fig. 8), which confirms the previous predictions [6]. At these small impact parameters, target excitation may be explained by a

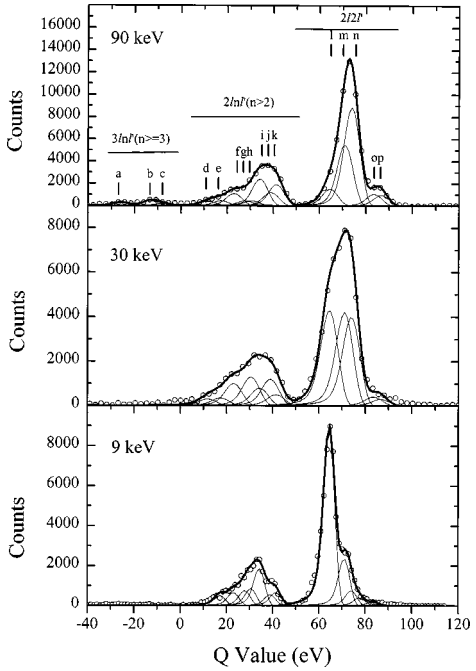

FIG. 9. Measured ADC Q-value spectra for the C^{5+}-He system. Different configurations $(a,b,c,\ldots)$ and corresponding Q values are given in Table IV.

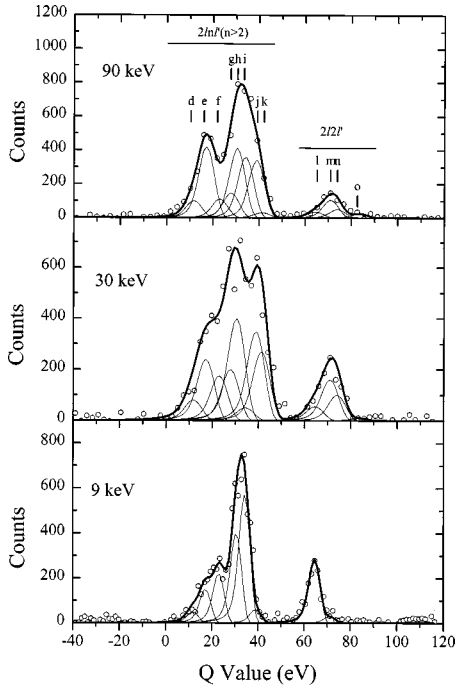

FIG. 10. Measured TDC Q-value spectra for the C^{5+}-He system. Different configurations $(a,b,c,\ldots)$ and corresponding Q values are given in Table IV.

TABLE IV. Different configurations and Q values involved in double electron capture for the C^{5+}-He system.

Peak	Configuration	Q value (eV)
a	$C^{3+}1s3dnl\ (n\sim\infty)$	−26
b	$C^{3+}1s3d^2$	−13.2
c	$C^{3+}1s3s^2$	−7.88
d	$C^{3+}1s2pnl\ (n\sim\infty)$	11.8
e	$C^{3+}1s2p5l$	17.2
f	$C^{3+}1s2p(^3P^0)4f(^2D)$	23.0
g	$C^{3+}1s2s(^3S)4d(^2D)$	27.9
h	$C^{3+}1s2p(^1P^0)3d(^2D)$	30.5
i	$C^{3+}1s2s(^1S)3d(^2D)$	34.2
j	$C^{3+}1s2s(^3S)3d(^2D)$	38.9
k	$C^{3+}1s2s(^3S)3p(^2P^0)$	41.3
l	$C^{3+}1s2p^2(^2S)$	64.5
m	$C^{3+}1s2p^2(^2D)$	71.0
n	$C^{3+}1s2s2p(^2P^0)$	74.0
o	$C^{3+}1s2s2p(^4P^0)$	83.5
p	$C^{3+}1s2s^2(^2S)$	86.6

TABLE V. ADC relative cross sections for the C^{5+}-He collision (%).

Peak	Configuration	90 keV	30 keV	9 keV
o,p	$1s2s^2(^2S)$; $1s2s2p(^4P^0)$	6.8±1.0	3.3±1.1	3.0±2.8
n	$1s2s2p(^2P^0)$	30.5±1.0	19.1±1.1	3.8±3.7
m	$1s2p^2(^2D)$	18.8±2.2	20.1±1.5	11.8±5.0
l	$1s2p^2(^2S)$	5.1±2.2	20.6±1.5	43.6±5.0
$d-k$	$1s2lnl'$ $(n\geqslant 3)$	28.6±3.3	26.1±6.7	29.1±9.4
a,b,c	$1s3lnl'$ $(n\geqslant 3)$	3.4±1.2	0	0

''recapture'' of one of the two molecular electrons by the target.

C. Double electron capture (DC)

TDC and ADC can be sorted by our RIMS by analyzing the projectile charge state. In each case, Q-value spectra are measured (Figs. 9 and 10). Populated configurations are listed in Table IV, and relative differential cross sections are given in Tables V and VI.

For the sake of simplicity, we avoid mentioning C^{3+} when we refer to the double capture configuration $C^{3+}(nln'l')$ in the following. As seen in Figs. 9 and 10, double electron capture populates mainly $(2lnl')$ states. For ADC, capture in the $(2l2l')$ state is dominant (60% of ADC). The measured ratios (TDC+ADC)/SC are 0.26 ±0.03, 0.43±0.05, and 0.26±0.03 for collision energies of 90, 30, and 9 keV, respectively.

The Q-value resolution is high enough to allow estimation of the population of the different $(2l2l')$ terms. In ADC, as the collision energy decreases, the term $1s2s2p\,^4P^0$, $1s2s^2\,^2S$, and $1s2s2p\,^2P^0$ states become weaker while the term $1s2p^2\,^2S$ population increases. The $1s2p^2\,^2D$ term population increases from 9 to 30 keV and then decreases between 30 and 90 keV collision energy. Concerning the $2lnl'$ $(n\geqslant 3)$ series, the relative cross section is not changed very much with the energy. This result confirms previous experimental results by Mann [14] and agrees with calculations by [6] and [7].

$(3lnl')$ $(n>3)$ series are only observed at 90 keV. It can be understood from the diabatic potential curves since the $(3lnl')$ $(n\geqslant 3)$ have no crossing with the entrance and the other single capture channel at large internuclear distance (Fig. 11). This result confirms again the deduction about reaction window spreading observed by Abdallah *et al.* [21].

TDC amounts to less than 2% of total double capture. For this process, $(2lnl')$ $(n\geqslant 3)$ states dominate the spectra. $(2l2l')$ states are weak in TDC while very strong in ADC. This is not surprising for this equivalent electron configuration, which is expected to be strongly autoionizing. This is confirmed by the measured stabilization ratio of the order of 2.5% (Table VII). In $(2l2l')$ states, it only clearly shows that the population of $1s2p^2(^2S)$ increases as the collision energy decreases. Again, the distribution allows us to estimate the relative cross sections of the different $(2lnl')$ states. The populations of $1s2pnl$ $(n\sim\infty)$, $1s2p5l$, $1s2p(^3p^0)4f(^2D)$, $1s2s(^3S)3d(^2D)$, and $1s2s(^3S)3p(^2P^0)$ decrease as the collision energy is decreased. The cross section for capture in $1s2s(^3S)4d(^2D)$, $1s2p(^1P^0)3d(^2D)$, and $1s2s(^1S)3d(^2D)$ states depends weakly on the collision energy.

Double capture on $(2l2l')$ states is the only one for which calculations have been performed [6,7]. Since we measure only relative cross sections, we compare the theoretical and experimental values through the dominant double and single capture channel ratio, namely $\sigma[C^{3+}(2l2l')]/\sigma[C^{4+}(3l)]$. Figure 12 shows that our results agree with [6] at 9 and 90 keV collision energy but with [7] at 30 keV. The experimental values lie in between the two calculations. The experiments evidence the existence of a maximum for this ratio around 2 keV/u, which is also produced by [6], but at an energy around 8 keV/u.

Since the cross sections relative to the configurations $(2lnl')$ $(n>2)$ are small, we only discuss here the angular behavior of the configuration $(2l2l')$ (Fig. 13), which is mainly visible in ADC spectra. Our measured scattering angle distributions confirm the measurement by [15]. Due to insufficient statistics for the TDC, we do not present any angular distributions. Schematic diabatic potential-energy curves are plotted in Fig. 11. The dominant single capture channel $(n=3)$ together with three main double capture subchannels, which lead to the symmetric $(2l2l')$ configurations labeled by l, m, and n (see Table IV), are plotted.

Two processes may be responsible for the double capture into $(2l2l')$ configurations: a two-step process via an $n=3$ single capture channel at an internuclear distance of about 8.4 and 1.0 a.u. (circles), or a one-step process at about 2.5 a.u. (squares). In the two-step process, first, one electron is captured on the M shell $(n=3)$ at large internuclear distance, then this electron is excited to the L shell $(n=2)$, while the second electron is captured in the L shell at a smaller internuclear distance ending as bound $(2l2l')$ states. This process due to dielectronic interaction is usually called the correlated transfer excitation (CTE) [27,28]. In the one-step process, the two electrons are simultaneously captured at about 2.5 a.u. It is noted that this two-electron transfer (CDC) is also governed by dielectronic interaction [28]. An alternative explanation has also been proposed by Laurent *et al.* [29]. They invoked a mechanism involving a virtual transition to the SC channel at the crossing followed by a

TABLE VI. TDC relative cross section for the C^{5+}-He collision (%).

Peak	Configuration	90 keV	30 keV	9 keV
$l-p$	$2l2l'$	0.7±0.1	1.7±0.2	1.5±0.1
$d-k$	$2lnl'$ $(n\geqslant 3)$	6.1±0.7	9.1±0.5	7.2±0.5
$a-c$	$3lnl'$ $(n\geqslant 3)$	0	0	0

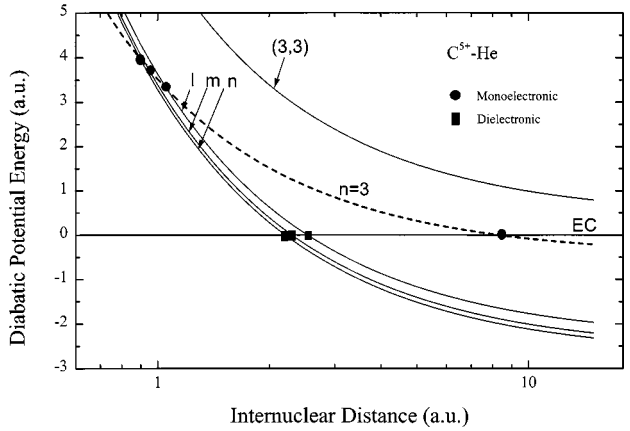

FIG. 11. Diabatic potential-energy curves of DC and SC presenting the different double capture pathways. ■, one-step; ●, two steps. *l*, *m*, and *n* are $C^{3+}[2p^2(^2S)]$, $C^{3+}[2p^2(D^2)]$, and $C^{3+}[2s2p(^2P^0)]$ DC channels, respectively; EC is entrance channel; 3 is the $C^{4+}(3l)$ SC channel; (3,3) is the $C^{3+}(3l3l')$ DC channel.

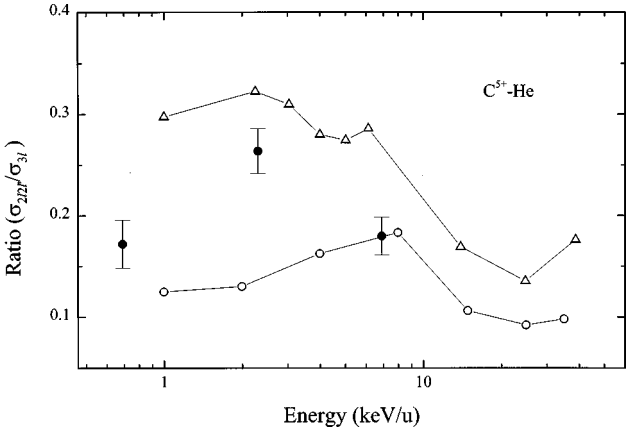

FIG. 12. Cross-section ratios between DC $C^{3+}(2l2l')$ and SC $C^{4+}(3l)$ for the C^{5+}-He system. ●, our experimental data; ○, Fritsch and Lin [6]; △, Tauljberg and Hansen [7].

transition in the DC channel. Such a mechanism may be active when the SC channel is in the neighborhood of the crossing between the DC channel and the entrance channel. This is not the case for the C^{5+}-He system.

We have calculated the classical angles corresponding to one and two steps according to the suggestion by Laurent *et al.* [29], These angles are simultaneously given in Fig. 13 in an $E\theta$ scale. It is expected that, for the diabatic transition, the location of the maximum of the scattering angle distribution is close to the classical threshold angle corresponding to the largest impact parameter. From Fig. 13, we can easily observe that the one-step process increases when the collision energy increases, as already mentioned in the C^{6+}-He system by Stolterfoht *et al.* [28], while the two-step process decreases with the increasing of collision energy. Comparing now the evolution of the peaks *l*, *m*, and *n* with the energy (in Fig. 9), we observe that the relative intensity of peak *m* remains roughly constant while the peak *l* increases and peak *n* decreases with the decrease of collision energy. So it can be deduced that, in our collision energy range, the term $1s2s2p(^2P^0)$ is mainly populated via the one-step process while $1s2p^2(^2S)$ and $(1s2p^2)(^2D)$ are mainly populated via the two-step process. Thus we can conclude that the configuration $(2l2l')$ is populated through the dielectronic interactions. Concretely, the populations of $1s2p^2(^2S)$ and $1s2p^2(^2D)$ are governed by CTE, while $1s2s2p(^2P^0)$ is governed by CDC. It is the first time, to our knowledge, that, for this system, we have evidence of the competition between one-step and two-step processes, which depends so strongly on the collision energy.

TABLE VII. Experimental stabilization ratios $\sigma_{TDC}/(\sigma_{TDC}+\sigma_{ADC})$ for the C^{5+}-He collision (%).

Peak	Configuration	90 keV	30 keV	9 keV
l–p	$2l2l'$	1.1±0.3	2.6±0.5	2.4±0.9
d–k	$2lnl'$ $(n\geqslant 3)$	17.6±4.0	25.8±6.7	19.8±6.8
a–c	$3lnl'$ $(n\geqslant 3)$	0		

IV. CONCLUSION

In conclusion, we have studied single and double electron capture using high-resolution RIMS, and it has been demonstrated again that RIMS is well-suited to get thorough details of the processes involved in the electron capture. For single capture, the $n=3$ state is dominating. The scattering angle resolution allows evidencing Stuckelberg oscillations. Spreading of the reaction window is confirmed; $n=2$ and 4 state contributions increase as the collision energy is raised.

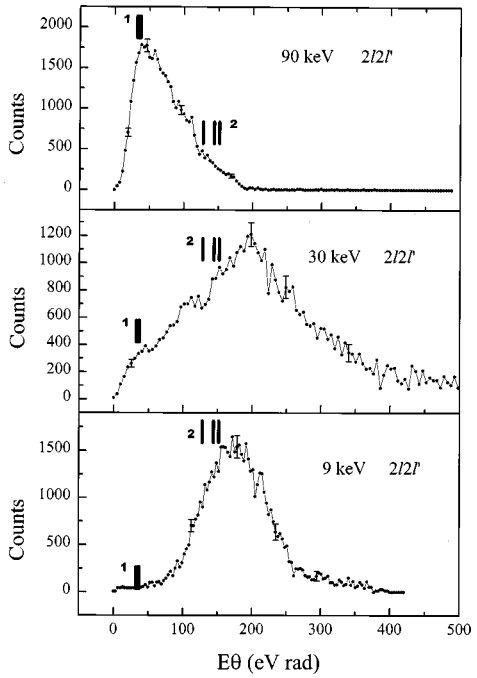

FIG. 13. Autoionizing double capture projectile scattering angle distributions for the $C^{3+}(2l2l')$ channel. The classical scattering angles for one step (1) and two steps (2) via $C^{4+}(3l)$ SC channel are also indicated. The angles of one step are close to each other. For two steps, from left the angles correspond to *l*, *m*, and *n* configurations.

The model proposed is able to reproduce qualitatively the scattering angle differential cross sections even for the $n=4$ state.

We have measured the TE contribution which is a factor of 3 smaller than the prediction [6]. However, the large associated scattering angles confirm the importance of small impact parameters in this process.

Double electron capture has been found mainly autoionizing due to a strong population of $(2l2l')$ states. The processes involved (one step and two steps) are identified through scattering angle distribution analysis. A strong collision energy dependence is evidenced for these processes. Furthermore, the Q-value resolution is high enough to reveal the processes contributing to the population of the $(2l2l')$ configurations: the dielectronic interaction is responsible for transfer to $(2l2l')$ configurations, the $1s2s2p(^2P^0)$ term is populated through a one-step process governed by correlated double capture (CDC), while the $1s2p^2(^2S)$ and $1s2p^2(^2D)$ terms are populated via the two-step process governed by correlated transfer excitation (CTE).

ACKNOWLEDGMENTS

We gratefully thank G. Grall for assistance in maintaining the computers. These experiments were performed at the Ganil facility, Caen, France.

[1] J. Ullrich, R. Moshammer, R. Dörner, O. Jagutzki, V. Mergel, H. Schmidt-Böcking, and L. Spielberger, J. Phys. B **30**, 2917 (1997).
[2] A. Cassimi, S. Duponchel, X. Flechard, P. Jardin, P. Sortais, D. Hennecart, and R. E. Olson, Phys. Rev. Lett. **76**, 3679 (1996).
[3] R. Dörner, V. Mergel, L. Spielberger, O. Jagutzki, J. Ullrich, and H. Schmidt-Böcking, Phys. Rev. A **57**, 312 (1998).
[4] X. Flechard, S. Duponchel, L. Adoui, A. Cassimi, P. Roncin, and D. Hennecart, J. Phys. B **30**, 3697 (1997).
[5] J. P. Hansen and K. Taulbjerg, Phys. Rev. A **45**, R4214 (1992).
[6] W. Fritsch and C. D. Lin, Phys. Rev. A **54**, 4931 (1994).
[7] J. P. Hansen and K. Taulbjerg, Phys. Rev. A **47**, 2987 (1993).
[8] T. Iwai, Y. Kaneko, M. Kimura, N. Kobayashi, S. Ohtani, K. Okuno, S. Takagi, H. Tawara, and S. Tsurubuchi, Phys. Rev. A **26**, 105 (1982).
[9] W. Waggoner, C. L. Cocke, L. N. Tunnell, C. C. Havener, F. W. Meyer, and R. A. Phaneuf, Phys. Rev. A **37**, 2386 (1988).
[10] K. Okuno, H. Tawara, T. Iwai, Y. Kaneko, M. Kimura, N. Kobayashi, A. Matsumoto, S. Ohtani, S. Takagi, and S. T. Tsurubuchi, Phys. Rev. A **28**, 127 (1983).
[11] M. G. Suraud, R. Hoekstra, F. J. de Heer, J. J. Bonnet, and R. Morgenstern, J. Phys. B **24**, 2543 (1991).
[12] R. A. Holt, M. H. Prior, K. L. Randall, R. Hutton, J. McDonald, and D. Schneider, Phys. Rev. A **43**, 607 (1991).
[13] M. H. Prior, R. A. Holt, D. Schneider, K. L. Randall, and R. Hutton, Phys. Rev. A **48**, 1964 (1993).
[14] R. Mann, Phys. Rev. A **35**, 4988 (1987).
[15] H. Khemliche, M. H. Prior, and D. Schneider, Phys. Rev. Lett. **74**, 5013 (1995).
[16] P. Sortais, Nucl. Instrum. Methods Phys. Res. B **98**, 508 (1995).
[17] X. Fléchard, Ph.D. thesis, Caen University of France, January, 1999 (unpublished); D. Hennecart, X. Fléchard, F. Frémont, A. Lepoutre, S. Duponchel, L. Adoui, and A. Cassimi, *Photonic and Atomic Collisions, Proceedings of the XXth ICPEAC* (World Scientific, Singapore, 1997), p. 557.
[18] R. D. Cowan, *The Theory of Atomic Structure and Spectra* (University of California Press, Berkeley, 1981).
[19] L. D. Landau, Phys. Z. Sowjetunion **2**, 46 (1932); C. Zener, Proc. R. Soc. London, Ser. A **137**, 696 (1932).
[20] A. Niehaus, J. Phys. B **19**, 2925 (1986).
[21] M. A. Abdallah, W. Wolff, H. E. Wolf, E. Y. Kamber, M. Stöckli, and C. L. Cocke, Phys. Rev. A **58**, 2911 (1998).
[22] C. Biedermann, H. Cederquist, L. R. Andersson, J. C. Levin, R. T. Short, S. B. Elston, J. P. Gibbons, H. Andersson, L. Liljeby, and I. A. Sellin, Phys. Rev. A **41**, 5889 (1990).
[23] E. Olson and A. Salop, Phys. Rev. A **14**, 579 (1976).
[24] E. L. Duman and B. Smirnov, Opt. Spectrosc. **32**, 234 (1972).
[25] C. Gaussorgues, R. C. Piacentini, and A. Salin, Comput. Phys. Commun. **10**, 223 (1975).
[26] H. Danared and A. Bárány, J. Phys. B **19**, 3109 (1986).
[27] H. Winter, M. Mack, R. Hoekstra, A. Niehaus, and F. de Heer, Phys. Rev. Lett. **58**, 957 (1987).
[28] N. Stolterfoht, C. C. Havener, R. A. Phaneuf, J. K. Swenson, S. M. Shafroth, and F. W. Meyer, Phys. Rev. Lett. **57**, 74 (1986).
[29] H. Laurent, M. Barat, M. N. Gaboriaud, L. Guillemot, and P. Roncin, J. Phys. B **20**, 6581 (1987).